

Sensing a Connection: Tree Distribution is Influenced by Deep Critical Zone Structure

Brady A Flinchum¹, Ciaran J Harman², and Donald Hagan¹

¹Clemson University

²Johns Hopkins University

March 04, 2024

Abstract

This study explores the impact of deep (>5 m) critical zone (CZ) architecture on vegetation distribution in a semi-arid snow-dominated climate. Utilizing seismic refraction surveys, we identified a significant correlation between saprolite thickness and LiDAR-derived canopy heights ($R^2=0.47$). We argue that CZ structure, specifically shallow fractured bedrock under valley bottoms, redirects groundwater to locations where trees are established—suggesting they are located in specific locations with access to nutrients and water. This work provides a unique spatially exhaustive perspective and adds to growing evidence that in addition to other factors such as slope, aspect, and climate, deep CZ structure plays a vital role in ecosystem development and resilience.

Hosted file

NLC_D9.docx available at <https://authorea.com/users/618679/articles/717376-sensing-a-connection-tree-distribution-is-influenced-by-deep-critical-zone-structure>

Hosted file

AGU_SuppInfo_Word_V1.docx available at <https://authorea.com/users/618679/articles/717376-sensing-a-connection-tree-distribution-is-influenced-by-deep-critical-zone-structure>

21 **Abstract**

22 This study explores the impact of deep (>5 m) critical zone (CZ) architecture on vegetation
23 distribution in a semi-arid snow-dominated climate. Utilizing seismic refraction surveys, we
24 identified a significant correlation between saprolite thickness and LiDAR-derived canopy
25 heights ($R^2=0.47$). We argue that CZ structure, specifically shallow fractured bedrock under
26 valley bottoms, redirects groundwater to locations where trees are established—suggesting they
27 are located in specific locations with access to nutrients and water. This work provides a unique
28 spatially exhaustive perspective and adds to growing evidence that in addition to other factors
29 such as slope, aspect, and climate, deep CZ structure plays a vital role in ecosystem development
30 and resilience.

31 **Plain Language Summary**

32 This study investigates how the hidden structure beneath the Earth's surface (called the critical
33 zone or CZ) affects where plants can grow and thrive. Using seismic refraction surveys, we
34 found that the critical zone structure correlates with tree distribution. Specifically, areas with
35 shallow fractured bedrock support the tallest trees. We argue that the shape of the critical zone
36 forces groundwater toward the surface, providing a steady water supply for trees during spring
37 and late summer. Our 1.5 km of seismic refraction data reveal a consistent pattern: trees are taller
38 when the fractured bedrock is close to the surface. This connection suggests that the influence of
39 critical zone structures on vegetation distribution in a given landscape may be as significant as
40 other factors such as slope, aspect, and climate.

41

42 **1 Introduction**

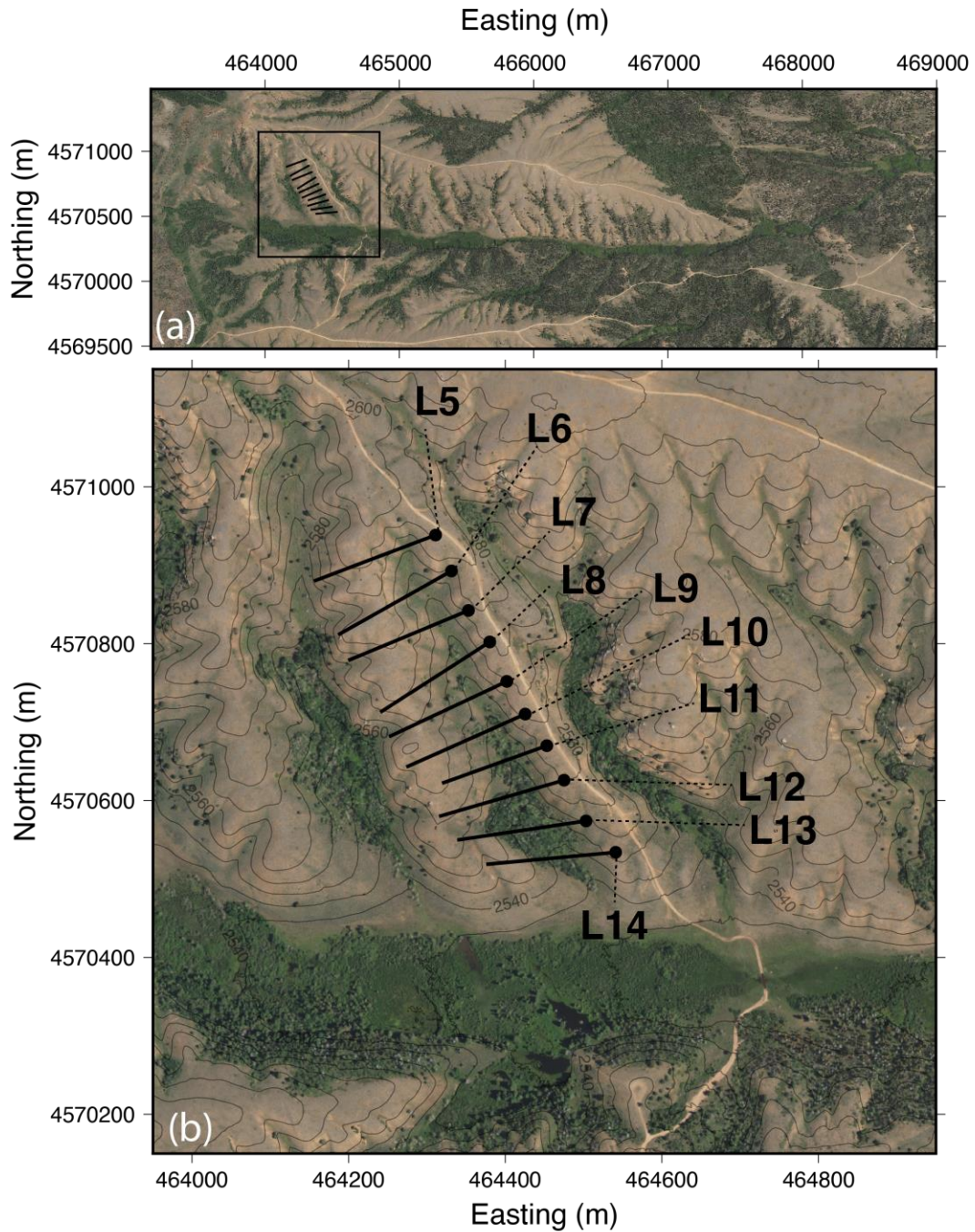
43 The critical zone (CZ) is the region near the Earth's surface created and maintained by
44 complex interactions between the atmosphere, hydrosphere, and biosphere, and spans from the
45 top of the canopy to fresh bedrock (S. L. Brantley et al., 2005; Susan L. Brantley et al., 2007). In
46 the CZ, rock is transformed into soil by physical and chemical weathering processes (Susan L.
47 Brantley, 2010; Gu et al., 2020; Lebedeva et al., 2007). This transformation releases critical
48 nutrients for plants and ecosystems (Arvin et al., 2017; Hahm et al., 2014; Uhlig et al., 2017;
49 Uhlig & Blanckenburg, 2019) while providing porosity for groundwater storage (Graham et al.,
50 1997; Hayes et al., 2019; Navarre-Sitchler et al., 2015). Here, we demonstrate evidence that deep
51 (>5 m) CZ architecture impacts the distribution of vegetation in semi-arid headwater watersheds
52 by influencing groundwater storage and flow.

53 This study was motivated by a clear and distinct pattern in vegetation visible in the
54 Laramie Range, just southeast of Laramie, Wyoming (Figure 1). This part of the Laramie Range,
55 classified as a semiarid rangeland, sits at an elevation between 2200 and 2700 m. The low-lying
56 areas are dominated by willows (*Salix* spp.), aspens (*Populus* spp.), and meadow grasses (Carey
57 et al., 2019; Carey & Paige, 2016). Aerial photographs provided by the National Agriculture
58 Imagery Program (NAIP) from July 2022 highlight the distinct vegetation patterns (Figure 1a).
59 In general, north-facing slopes tend to have more vegetation, and many of the first-order
60 drainages appear to support thick stands of vegetation (Figure 1a). However, not all first-order
61 drainages exhibit dense vegetation, suggesting another process might be important in vegetation
62 distribution across this landscape (Figure 1).

63 Previous studies have examined relationships between vegetation density and surface
64 topographic attributes such as slope, aspect, and relief (Emanuel et al., 2014; Gillieson et al.,

65 1996; Marston, 2010). However, few have examined the role of subsurface topography. Here, we
66 use shallow seismic refraction surveys to characterize relationships between vegetation density
67 and deep CZ structure. Seismic refraction surveys generate profiles of seismic velocity tens of
68 meters deep and hundreds to thousands of meters long (Flinchum et al., 2022; Uecker et al.,
69 2023). The strong relationship between seismic velocity and porosity means these images can
70 indicate the depth and degree of weathering in landscapes underlain by crystalline bedrock
71 (Callahan et al., 2020; Hayes et al., 2019; Holbrook et al., 2014). In recent years, seismic
72 refraction has allowed CZ architecture to be characterized over large spatial scales in various
73 lithologies and climates (Donaldson et al., 2023; Huang et al., 2021; Leone et al., 2020; Pedrazas
74 et al., 2021).

75 The seismic refraction velocities presented here are correlated with vegetation height
76 ($R^2=0.47$), suggesting a connection between existing CZ structure and the distribution of trees.
77 We hypothesize that the shallow bedrock under the tallest canopy forces groundwater to the
78 surface under these drainages. The presence of shallow fractured bedrock prevents water loss
79 during the spring melt and redirects older water from higher in the watershed into the valley
80 bottoms, providing a reservoir of water and nutrients for the trees throughout the growing season.



81

82 *Figure 1* Map of the study area. The image is an aerial photograph from the National
83 *Agricultural Image Program (NAIP)* taken on July 2, 2022, and topographic contours are
84 *derived from 1 m LiDAR data. Dots are the start of seismic profiles.*

85 **2 Materials and Methods**

86 **2.1 Study Site**

87 We collected 1.5 km of seismic refraction data in a small North/South trending valley
88 (which we will refer to as V1) defined by interfluves with approximately 20 m of relief (Figure
89 1a). V1 has an ephemeral stream and drains into North Lodgepole Creek, a perennial stream with
90 numerous beaver ponds along its reach, flowing approximately east-west in our study area
91 (Figure 1a). There is a notable stand of quaking aspen trees (*Populus tremuloides* Michx.) at the
92 outlet of V1 (Figure 1b). As the valley climbs in elevation, the trees give way to shrub-steppe
93 and grassland vegetation. In the Laramie Range, these isolated and patchy stands of trees persist,
94 whereas another stand exists in the valleys to the east and the west (Figure 1b). Given the
95 patchiness of the vegetation, we set up geophysical surveys to determine if the locations of the
96 trees were associated with the CZ structure.

97 The study site is part of a gentle undulated topography on the Rocky Mountain erosional
98 surface (Chapin & Kelley, 1997; Eggler et al., 1969; Evanoff, 1990). Erosion rates from
99 cosmogenic nuclides suggest that this surface erodes at a rate that will replace the gently rolling
100 hills every 1 to 2 million years (Dethier et al., 2014). The NLC site is non-glaciated granitic
101 terrain and relatively undisturbed by human land use. Ten years of local climate data from the
102 Crow Creek SNOTEL station (~2 km south) show the site has a mean annual temperature of 5.4
103 °C and receives 620 mm of annual precipitation, where 90% of the precipitation is recorded as
104 snow (Natural Resources Conservation Service (NRCS), 2015).

105 There are two well-known study sites nearby where we can leverage existing
106 observations. The Three Little Valleys site is 5 km south of the NLC site and is of the same
107 geology with similar, distinct asymmetrical slopes and vegetation cover (Uecker et al., 2023).

108 Despite the apparent asymmetrical contrast, Uecker et al. (2023) collected 3.9 km of seismic
109 refraction data and showed that the depth to bedrock could be greater than 60 m and argued that
110 trees on the north-facing slopes are preferentially located to obtain more water based on
111 differences in P-wave velocity (Uecker et al., 2023). Another well-studied site is the Blair-Wallis
112 (BW) located 12 km south (Flinchum, Holbrook, Grana, et al., 2018; Flinchum et al., 2019;
113 Keifer et al., 2019; Pasquet et al., 2021; Wang et al., 2019). At BW, the CZ was reported to be
114 upwards of 60 m thick under ridges but only 2-3 m thick under valley bottoms. At BW, inverted
115 bedrock topography was observed and fits well with a regional stress model under regional
116 compressive stress (Flinchum, Holbrook, Rempe, et al., 2018).

117

118 **2.2 Seismic Refraction**

119 The seismic profiles presented were acquired in 2015 using Geometrics Geodes and 144
120 or 168 geophones at 1-meter spacing. Shots were collected using a sledgehammer, and the
121 spacing varied between 5 and 10 meters. Each shot was stacked 5 and 8 times to increase the
122 signal to noise. Topographic profiles were extracted from 1-meter resolution LiDAR data
123 collected by the Wyoming Center for Hydrology and Environmental Geophysics (WyCEHG) in
124 2014.

125 We manually picked the first arrivals in Python. We were conservative, omitting channels
126 where the first arrival was unclear. Most of the arrivals were picked without a filter. However, a
127 band-pass filter (20-150 Hz) was used to pick the farthest offset arrivals. We used reciprocal
128 travel times to ensure we picked the same phase of the first arrival. We used the refraction
129 package in the Python Geophysical Inversion Modeling Library (PyGIMLi) to invert the first
130 arrival times (Rücker et al., 2017). The forward model assumes the elastic energy travels as rays.

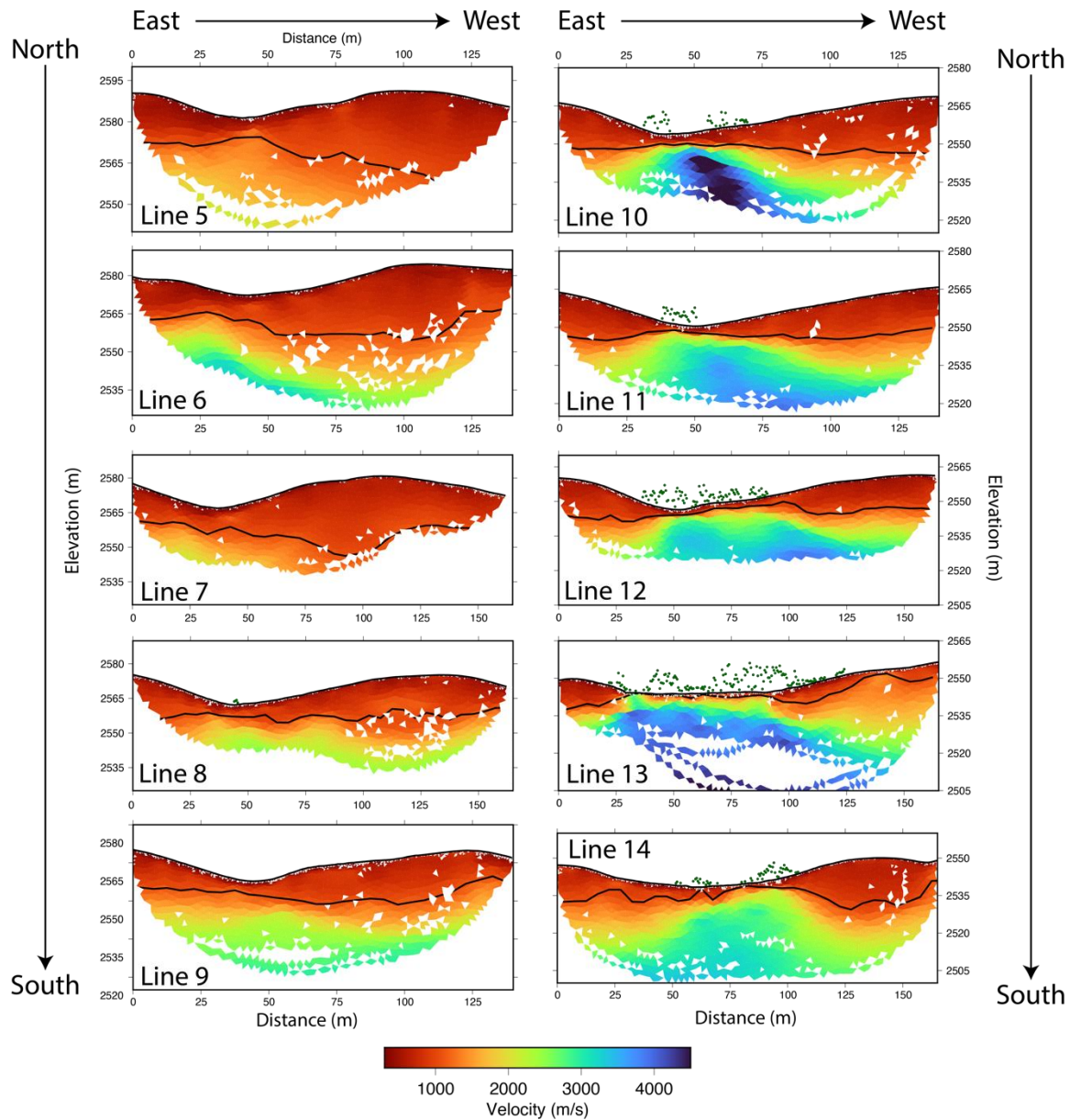
131 This assumption allows the package to use a computationally efficient shortest path algorithm
132 (Dijkstra, 1959; T. Moser, 1991; T. J. Moser et al., 1992). The inversion uses a deterministic
133 Gauss-Newton scheme that minimizes the χ^2 error. To compute the χ^2 error, every arrival time
134 must have an associated uncertainty value. These assigned uncertainty values have a large weight
135 in the final solution. Here, we assigned uncertainties using a linear interpolation based on the
136 distance between the source and the receiver. At small offsets, we assign a small uncertainty (~1
137 ms); at larger offsets, we assign a larger uncertainty (~3 ms). This interpolation of the
138 uncertainty emphasizes our ability to better pick arrivals from near offsets because of signal-to-
139 noise in the data (B. Flinchum et al., 2021; B. A. Flinchum et al., 2020).

140 **3 Results**

141 **3.1 Seismic Refraction**

142 The velocities in the profiles increase from the top to the bottom of the V1 watershed
143 (e.g., north to south) (Figure 2). In the upper parts of the watershed, the profiles are characterized
144 by low ($V_p < 1200$ m/s) seismic velocities that extend greater than 20 m into the subsurface
145 (Figure 2). In our data set, it is rare to encounter velocities greater than 3000 m/s. L10 is the only
146 profile that shows velocities greater than 4000 m/s (Figure 2). The highest velocities in L10
147 occur at the valley bottom. However, they are slightly offset to the west relative to the center of
148 the drainage and have an asymmetrical shape with an apparent dip to the west. Moving further
149 south and closer to the exit of the watershed, the velocities never exceed 4000 m/s, but the high-
150 velocity anomaly ($V_p > 3000$ m/s) comes closer to the surface while spanning the valley bottom
151 (Figure 2).

152 L13 shows there is a recognizable shift in subsurface structure, where the high velocities
153 ($V_p > 3000$ m/s) come close (<1-2 m) to the surface and then stay present for approximately 75
154 m (Figure 2). On L13, the sharp lateral gradients remain sharp on the east but also become well-
155 defined and sharp on the west (Figure 2). On L14, the high-velocity region weakens, but the
156 asymmetry switches directions. Hence, the high-velocity anomaly appears to dip to the east and
157 is bound to the west by a lateral gradient while the east gently tapers off (Figure 2). L10, the one
158 with the highest velocities, marks the onset of the stand of trees. The stand of trees spans the
159 entire valley at the same location where the high-velocity anomaly is the shallowest and most
160 continuous on the surface along L13 (Figure 2). The spatial plots illustrate that the northernmost
161 profiles lose the higher velocities but also get slower, where velocities greater than 1200 m/s are
162 almost absent on the northernmost profile (L5).



163

164 *Figure 2 Seismic refraction results for all profiles in the first-order drainage. All profiles are*

165 *masked by ray coverage. The solid black line plotted in each profile is the 1200 m/s contour.*

166 *Green dots are extracted from the vegetation heights at 1 m resolution. The profiles are*

167 *organized from north (Line 5) to south.*

168

169 **3.2 Saproilite Thickness and Canopy Heights**

170 Boreholes and soil pits were not available to interpret the seismic velocities, so we rely
171 on results from BW (Flinchum et al., 2019; Flinchum, Holbrook, Grana, et al., 2018; Keifer et
172 al., 2019; Pasquet et al., 2021; Wang et al., 2019). At BW, 13 Geoprobe and deep wells were
173 drilled, and the depth of refusal of the Geoprobe or the casing depth of the larger holes occurred
174 at a velocity of 1100 +/- 180 m/s (mean and standard deviation) (Flinchum, Holbrook, Grana, et
175 al., 2018; Flinchum, Holbrook, Rempe, et al., 2018). Since our site is in a similar climate on the
176 same lithology, we interpret the 1200 m/s velocity contour to mark the bottom of the saprolite.
177 Seismic refraction profiles conducted on granites in the Laramie Range (Flinchum, Holbrook,
178 Rempe, et al., 2018) and Southern Sierra Nevada Mountains (Holbrook et al., 2014) show that
179 unfractured bedrock should have a velocity of ~4000 m/s.

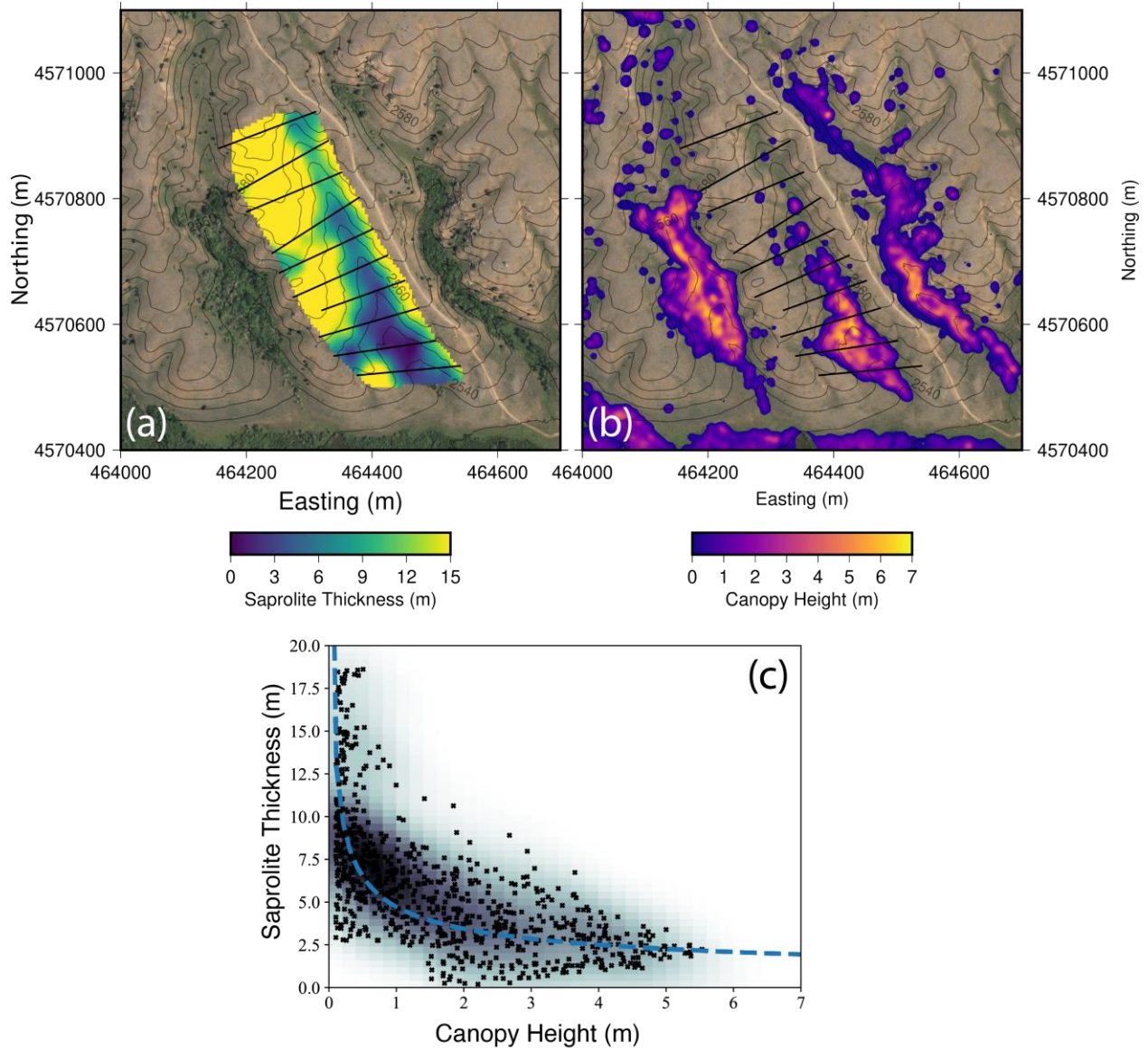
180 We extracted the depth to 1200 m/s along each profile to mark the boundary dividing
181 saprolite and fractured rock. Then, we used a continuous curvature spline (Smith & Wessel,
182 1990) to construct a saprolite thickness map of a rectangular region around our profiles (Figure
183 3a). The data were interpolated to a 5x5 meter grid. We applied a 7 m Gaussian smoothing filter
184 to the vegetation height to smooth out the canopy (Figure 3b) and interpolated the smooth
185 canopy heights to a 5x5 meter grid to investigate the visible correlations between saprolite
186 thickness and canopy height (Figure 3c). The interpolated saprolite thickness maps show that the
187 saprolite thins as the trees get taller (Figure 3). The relationship with the canopy height appears
188 to be a power relationship ($a = 4.72$; $b = -0.46$) with a stronger negative correlation in log-log
189 space as opposed to linear space ($R_{\log\text{-log}} = -0.68$ versus $R_{\text{linear}} = -0.60$) (Figure 3). The stand of
190 trees is tallest along L11, L12, and L13, and, vegetation taller than 5 m is present on L10 through
191 L14. The saprolite starts to thin at L10, which marks the onset of the large stand of trees. The

192 thinnest saprolite occurs along L13 and is less than 2 m thick for over 75 m along the valley
193 bottom, which is also the widest and tallest location where the trees are usually greater than 7-8
194 m tall (Figure 3).

195 Our seismic refraction data in V1 rarely encounter velocities greater than 4000 m/s
196 (Figure 2). This is anomalous because TLV and BW (5 km and 12 km south) show velocities
197 greater than 4000 m/s (Flinchum, Holbrook, Rempe, et al., 2018). The lack of velocities greater
198 than 4000 m/s suggests that we only observe unfractured bedrock under L10 (Figure 2). The lack
199 of bedrock is not necessarily a function of our profile lengths since the smallest profiles were still
200 140 m long and previous work images bedrock with similar profile lengths (Flinchum, Holbrook,
201 Rempe, et al., 2018; Uecker et al., 2023). The low velocities (<1200 m/s) suggest that the
202 material at the top part of the drainage is weathered and likely has 25-35% porosities based on
203 samples from BW (Flinchum, Holbrook, Grana, et al., 2018).

204 Given the similar climate, similar lithology, and similar relief, we assume that the water
205 table is similarly flat at V1 (e.g., deeper under ridges and shallow under valleys). If an increase
206 in saturation caused the increase in velocity, we would observe higher ($V_p > 1500$ /s) velocities
207 below the elevation of the valleys under the ridges (Figure 2). Second, the water table and
208 saprolite boundary were co-located at the BW based on six kilometers of seismic refraction data,
209 eight boreholes, 13 Geobrobe samples, and surface and nuclear magnetic resonance soundings.
210 The surface and borehole NMR showed perched water tables in topographic depressions in the
211 fractured bedrock topography (see Fig. 11 in (Flinchum et al., 2019)). Recently, data from BW
212 was imaged with full waveform inversions, showing that the saprolite and fractured bedrock
213 boundary is sharp but laterally heterogeneous (Eppinger et al., 2024). Given the proximity,
214 shared climates and lithologies, and identical geophysical tools used to characterize the CZ at

215 both sites, we assume a similar interpretation: velocities more significant than 1200 m/s indicate
216 fractured bedrock and not necessarily fully saturated saprolite and the water table is near the
217 vertically sharp but laterally heterogeneous boundary.



218

219 *Figure 3. Saprolite thickness and canopy heights. (a) Interpolated depth to saprolite ($V_p = 1200$*
 220 *m/s). The seismic refraction profiles are shown as thick black lines. 5 m topographic contours*
 221 *are also shown. (b) Canopy height after being passed through a 7x7 m smoothing filter. (c)*
 222 *Scatter plot of vegetation height (panel b) versus saprolite thickness (panel a). The 2D*
 223 *probability density function is a color map behind the data points. The blue dashed line is the*
 224 *power law fit ($y = ax^b$; $a = 4.72$; $b = -0.46$; $R^2 = 0.47$). (d) Saprolite thickness from the Blair*

225 *Wallis site 12 km south derived from seismic refraction lines. This is modified from Figure 12a*

226 *in Flinchum et al. (2018).*

227

228 **4 Discussion**

229 Much of the vegetation visible in the NAIP imagery is created by trees (Figure 1). Trees
230 play an essential role in CZ development by connecting the atmosphere and the soil (Susan L.
231 Brantley et al., 2017). They drive energy, water, and nutrient cycles that shape the CZ and soils
232 over geologic timescales (Gabet & Mudd, 2010; Pawlik et al., 2016). In granitic landscapes that
233 share climate, the phosphorus in the underlying bedrock is correlated with tree density,
234 suggesting that trees may preferentially locate themselves near bedrock where they can access
235 critical limiting nutrients (Hahm et al., 2014). The connection between tree density and
236 underlying lithology and soil properties is well studied; for example, in Spain, elevation and
237 lithology are the two variables that best predict maritime pine growth potential (Eimil-Fraga et
238 al., 2014). In the southern Appalachians, depth to bedrock is a reliable predictor of forest
239 productivity, as shallow bedrock confines the root systems of trees to a thin layer of topsoil
240 (Carter et al., 2000). Similarly, bedrock composition (e.g. porosity, nutrient content) has been
241 shown to influence the susceptibility of trees to water stress, especially in areas that experience
242 periodic droughts (Callahan et al., 2022).

243 In addition to nutrient limitations, there is a strong connection between vegetation
244 patterns and water availability (Banks et al., 2009; Chiloane et al., 2022; Jones et al., 2020).
245 Evapotranspiration from stomatal pores in leaves, driven by the relatively low vapor pressure of
246 air, creates suction – passively drawing water from the soil and into and through the xylem
247 tissues in roots, stems and leaves (Lambers et al., 2008). Water's movement depends upon
248 evapotranspiration's ability to generate enough negative pressure to overcome the gravitational
249 potential and the matric potential of water held tightly in soil pores (Lambers et al., 2008). For
250 non-wetland tree species, it is critical that the rooting zone not be fully saturated because the

251 stems of these species typically lack specialized aerenchyma tissues to transmit oxygen from
252 above ground and thus must rely on oxygen from soil pores to satisfy their belowground
253 respiratory demands (Koch et al., 2004). Therefore, for certain species to survive, many require
254 easy access to water (e.g., well-drained soils) but cannot stay if they remain saturated year-round.

255 In forested uplands, tree roots are confined to the first few meters of the CZ (Canadell et
256 al., 1996; Fan et al., 2017; Jackson et al., 1996); but recent work also shows they depend on
257 deeper water in the fractured rock to survive long summers (McCormick et al., 2021; Rempe &
258 Dietrich, 2018; Salve et al., 2012) and there are documented connections between vegetation
259 density and hillslope stream connectivity (Emanuel et al., 2014). Regions of topographic
260 convergence are usually associated with groundwater-dependent ecosystems because they are
261 discharge zones that have the most impact on nutrient and water availability (Tai et al., 2020).
262 This dependence on groundwater is well known, and many studies have investigated
263 groundwater-dependent ecosystems (Chiloane et al., 2022). Trees' dependence on water has
264 made it possible to use tree height as a metric to predict groundwater depth (Yang et al., 2019).
265 Since the underlying CZ structure substantially impacts local groundwater flow paths, the
266 presence or lack of trees could be used to predict the underlying CZ structure because they mark
267 locations where conditions are optimal for their survival.

268 The stands of trees must have access to nutrients and water. The re-direction of water by
269 bedrock is 3-dimensional, which is difficult to convey but is essential for a complete
270 understanding of the system (Figure 4). In the north-south-oriented V1 drainage, the subsurface
271 topographic gradients suggest that flow direction is primarily down the drainage (e.g., N/S flow
272 perpendicular to the seismic profiles) rather than laterally from the ridges to the valley (i.e., E/W
273 flow along the seismic profiles). Lateral flow into V1 and the surrounding valleys would only

274 occur if the water table were high enough under the ridges. In the small watershed where the
275 trees are located, most water would travel from the north to the south before being redirected at
276 the valley outlet to the west to flow along the regional topographic gradient out of the Laramie
277 Range (Figure 1a). Our seismic data suggest that the fractured bedrock rises near the surface
278 abruptly starting at L10, coinciding with the trees' beginning (Figure 2). This interpreted
279 decrease in porosity and permeability under the valley would cause groundwater traveling from
280 the north to the south to be directed toward the land surface.

281 The importance of bedrock in controlling vegetation distribution has been observed
282 elsewhere. Different lithologies, such as large sandstone blocks embedded into a *mélange*, have
283 different CZ thicknesses and thus different water storage capabilities, resulting in dramatic visual
284 differences in vegetation distribution in California (Hahm et al., 2019). Additionally, more and
285 more observations, both remote sensed (McCormick et al., 2021) and local measurements
286 (Schmidt & Rempe, 2020), show that trees depend on, and thus access, water stored in the
287 fractured rock layer below the soil—which has recently been termed rock moisture (Rempe &
288 Dietrich, 2018; Salve et al., 2012).

289 In the Laramie range, the presence of trees decreases the wind velocity, allowing snow to
290 pile up in the stands while reducing the incoming solar radiation by shading the snowpack (He et
291 al., 2019). Thus, snow accumulates in the valley bottoms, especially in those valley bottoms with
292 stands of trees. The presence of shallow fractured bedrock impacts water availability in two ways
293 (Figure 4). First, the low permeability and porosity under the valley bottoms would restrict
294 regional or local groundwater flow to shallow depths at the valley bottoms (perhaps even
295 exfiltrating there), where it could be accessed by the trees (Figure 4). Second, fractured bedrock
296 typically has a minor drainable porosity, so less recharge is needed to raise the water table within

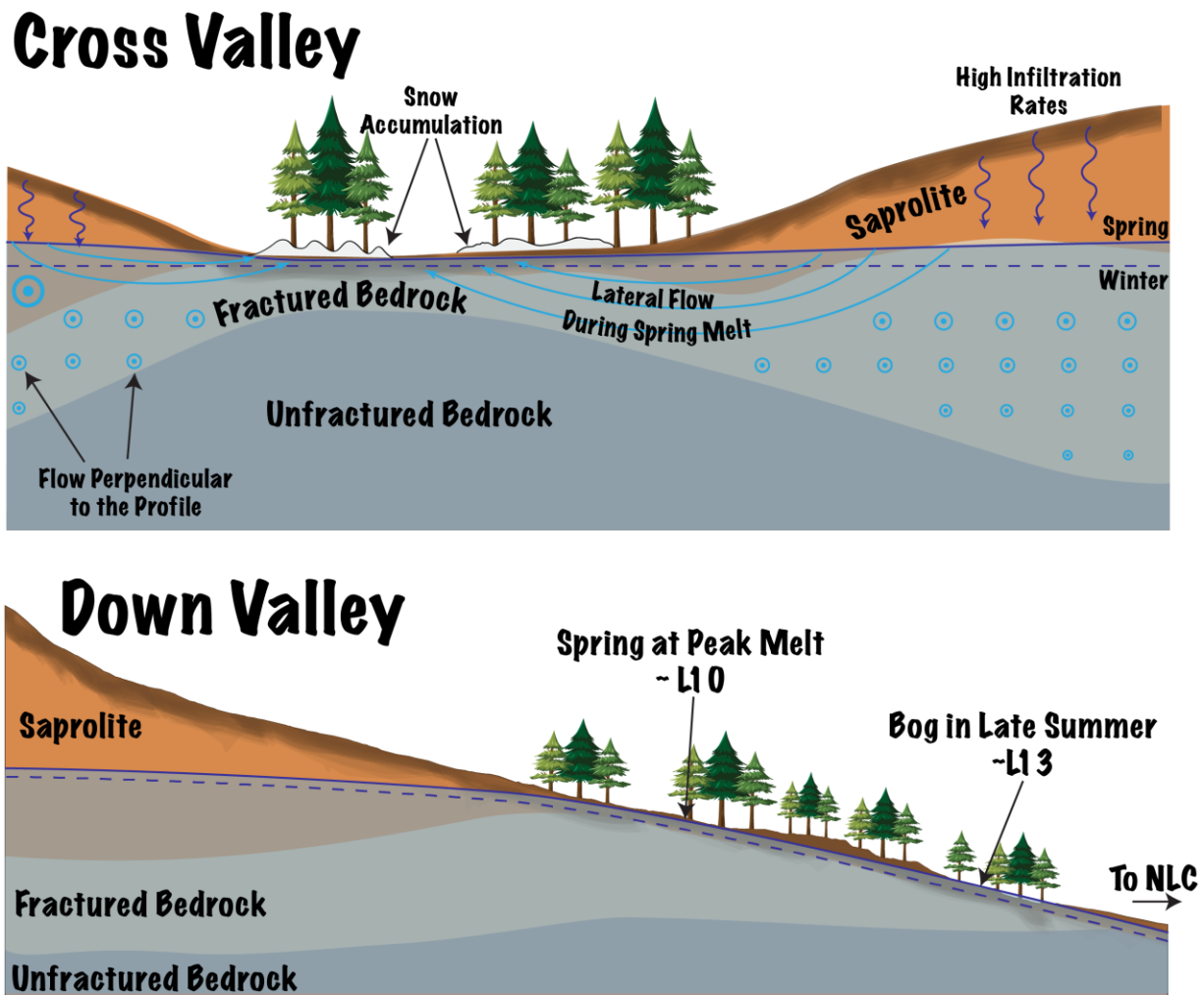
297 the fractured rock. This would result in a higher water table and thus more available to plants
298 despite the semi-arid conditions. Thus, the initial pulse of snowmelt would effectively behave
299 similarly to a perched aquifer, providing the most water in well-drained soils during the peak of
300 the growing season. Then, the CZ architecture re-directs local north-south flow upward into the
301 valley, providing groundwater to sustain the trees in the late summer (Figure 4).

302 Further evidence of the influence of the bedrock on water availability is given by the
303 presence of a saturated bog along L14 from 55 to 105 and 35 m to 120 m along L13 in mid-
304 summer (recorded in the field notes by the team in late July) (Figure 2). This bog is unlikely to
305 be due to low permeability surface soils. Infiltration tests in sagebrush-covered areas (mostly
306 hilltops) throughout the Laramie Range have shown that overland flow under natural conditions
307 is rare because of the high infiltration capacity of the soils (Carey & Paige, 2016). The strong
308 association between the trees and the presence of a bog in mid-summer suggests that the deeper
309 CZ architecture is responsible for providing water and nutrients required by the trees. In
310 particular, Quaking aspen is a highly water-demanding species that grows best in porous, well-
311 drained soils with water tables between 0.6 and 2.5 m (Perala et al., 1990). Additionally, its
312 seeds, which are dispersed in late spring/early summer, require a period of contact with heavily
313 saturated soils to germinate (Perala et al., 1990). The high water demand and the need for wet
314 soils to grow suggest they would not thrive in a semi-arid environment that favors shrub or
315 grassland vegetation. However, the deep CZ structure has provided the right conditions,
316 suggesting that aspen might serve as an “indicator species” (see Clements, 1924) that could be
317 used to estimate saproilte thickness.

318 Figure 4Figure 3Figure 3Figure 3Figure 3Figure 3

319

320



321

322 *Figure 4 CZ and hydrological conceptualization, both sections are vertically exaggerated and*
 323 *not to scale. (a) Cross-section across the valley based on L13 from Figure 2. In the cross-section*
 324 *view, the water flowing perpendicular to the page is dominant, especially in the winter. The*
 325 *water table rises during spring melt, during lateral flow to the trees, and the shallow fractured*
 326 *bedrock keeps the snow melt close to the trees during the spring. (b). Down valley view.*

327

328 **5 Conclusions**

329 The results presented here provide a unique perspective on the complex connections between
330 vegetation distribution and deep CZ architecture. Our data suggest that the trees in the Laramie
331 Range are restricted to areas with thinner saprolite. We argue that the shallow fractured bedrock
332 structure would impact the local and regional groundwater flow patterns that would work to the
333 advantage of the trees. The power law displayed in our data ($R^2 = 0.47$) is more evidence to
334 suggest that in addition to other factors such as slope, aspect, and climate, the deep CZ structure
335 plays a vital role in ecosystem development and resilience. Our results also support the idea of
336 trees as “indicator species” for deep CZ architecture, as their presence and size reflect a unique
337 combination of environmental and CZ factors that otherwise require sophisticated and/or labor-
338 intensive techniques to measure. The results highlight the importance of dynamic and complex
339 connections between ecosystem development, the underlying geology, and deep (> 5 m) CZ
340 architecture. Although more work can be done to ground truth in the geophysical data, the
341 spatially exhaustive observations created by seismic refraction can provide observational data of
342 CZ structures over large areas to help our understanding of CZ processes.

343 **Acknowledgments**

344 We are grateful to the many undergraduate researchers who helped collect the seismic refraction
345 data for this project as part of the Wyoming Center for Environmental Hydrology and
346 Geophysics (WyCEHG) team under the guidance of Matthew Provar, Bradley J. Carr, and W.
347 Steven Holbrook. We are also grateful to the broader CZ community for providing stimulating
348 conversations over many years that have helped shape the narrative of this manuscript—
349 specifically connecting the deep and often inaccessible CZ to observations we can make on the

350 surface. This study was supported by the National Science Foundation award “Collaborative
351 Research: Network Cluster: Bedrock controls on the deep critical zone, landscapes, and
352 ecosystems” (NSFEAR 2012357, NSFEAR 2012227, NSFEAR 2012353) and “Water in a
353 Changing West: The Wyoming Center for Environmental Hydrology and Geophysics” (NSFEPS
354 1208909). Data used for this manuscript can be found and downloaded on Hydroshare:

355 **Open Research**

356 The data used for this manuscript can be found and downloaded on Hydroshare: Flinchum, B.
357 A. (2024). Supporting Data Repository for Sensing a Connection: Tree Distribution is Influenced
358 by Deep Critical Zone Structure, HydroShare,
359 <http://www.hydroshare.org/resource/56d30051589b4a5ca0cbb146eae711d3>

360

361

362 **References**

363

364

365 Arvin, L. J., Riebe, C. S., Aciego, S. M., & Blakowski, M. A. (2017). Global patterns of dust and
366 bedrock nutrient supply to montane ecosystems. *Science Advances*, 3(12), eaao1588.

367 <https://doi.org/10.1126/sciadv.aao1588>

368 Brantley, S. L., White, T. S., Sparks, D. L., Richter, D. D., Pregitzer, K. S., Derry, L. A., et al.

369 (2005). *Frontiers in Exploration of the Critical Zone: Report of a workshop sponsored by the*
370 *National Science Foundation (NSF)* (p. 30).

371 Brantley, Susan L. (2010). Rock to regolith. *Nature Geoscience*, 3(5), 305–306.

372 <https://doi.org/10.1038/ngeo858>

373 Brantley, Susan L., Goldhaber, M. B., & Ragnarsdottir, K. V. (2007). Crossing Disciplines and
374 Scales to Understand the Critical Zone. *Elements*, 3(5), 307–314.

375 <https://doi.org/10.2113/gselements.3.5.307>

376 Callahan, R. P., Riebe, C. S., Pasquet, S., Ferrier, K. L., Grana, D., Sklar, L. S., et al. (2020).

377 Subsurface Weathering Revealed in Hillslope-Integrated Porosity Distributions. *Geophysical*
378 *Research Letters*, 47(15). <https://doi.org/10.1029/2020gl088322>

379 Carey, A. M., & Paige, G. B. (2016). Ecological Site-Scale Hydrologic Response in a Semiarid
380 Rangeland Watershed. *Rangeland Ecology & Management*, 69(6), 481–490.

381 <https://doi.org/10.1016/j.rama.2016.06.007>

- 382 Carey, A. M., Paige, G. B., Carr, B. J., Holbrook, W. S., & Miller, S. N. (2019). Characterizing
383 hydrological processes in a semiarid rangeland watershed: A hydrogeophysical approach.
384 *Hydrological Processes*, 33(5), 759–774. <https://doi.org/10.1002/hyp.13361>
- 385 Chapin, C. E., & Kelley, S. A. (1997). Chapin and Kelley - 1997 - The Rocky Mountain erosion
386 surface in the front ra.pdf. Retrieved from
387 http://archives.datapages.com/data/rmag/geohistfrontrange1997/chapin_b.pdf
- 388 Dethier, D. P., Ouimet, W., Bierman, P. R., Rood, D. H., & Balco, G. (2014). Basins and
389 bedrock: Spatial variation in ^{10}Be erosion rates and increasing relief in the southern Rocky
390 Mountains, USA. *Geology*, 42(2), 167–170. <https://doi.org/10.1130/g34922.1>
- 391 Donaldson, A. M., Zimmer, M., Huang, M. -H., Johnson, K. N., Hudson-Rasmussen, B.,
392 Finnegan, N., et al. (2023). Symmetry in Hillslope Steepness and Saprolite Thickness
393 Between Hillslopes With Opposing Aspects. *Journal of Geophysical Research: Earth*
394 *Surface*, 128(7). <https://doi.org/10.1029/2023jf007076>
- 395 Egger, D. H., Larson, E. E., & Bradley, W. C. (1969). Granites Grusses and Sherman Erosion
396 Surface Southern Laramie Range Colorado-Wyoming. *American Journal of Science*, 267(4),
397 510-.
- 398 Emanuel, R. E., Hazen, A. G., McGlynn, B. L., & Jencso, K. G. (2014). Vegetation and
399 topographic influences on the connectivity of shallow groundwater between hillslopes and
400 streams. *Ecohydrology*, 7(2), 887–895. <https://doi.org/10.1002/eco.1409>

- 401 Evanoff, E. (1990). Early Oligocene paleovalleys in southern and central Wyoming: Evidence of
402 high local relief on the late Eocene unconformity. *Geology*, 18(5), 443–446. Retrieved from
403 <http://geology.gsapubs.org/content/18/5/443.short>
- 404 Flinchum, B. A., Holbrook, W. S., Rempe, D., Moon, S., Riebe, C. S., Carr, B. J., et al. (2018).
405 Critical Zone Structure Under a Granite Ridge Inferred From Drilling and Three-Dimensional
406 Seismic Refraction Data. *Journal of Geophysical Research: Earth Surface*, 123(6), 1317–
407 1343. <https://doi.org/10.1029/2017jf004280>
- 408 Flinchum, B. A., Holbrook, W. S., Grana, D., Parsekian, A. D., Carr, B. J., Hayes, J. L., & Jiao,
409 J. (2018). Estimating the water holding capacity of the critical zone using near-surface
410 geophysics. *Hydrological Processes*, 32(22), 3308–3326. <https://doi.org/10.1002/hyp.13260>
- 411 Flinchum, B. A., Holbrook, W. S., Parsekian, A. D., & Carr, B. J. (2019). Characterizing the
412 Critical Zone Using Borehole and Surface Nuclear Magnetic Resonance. *Vadose Zone*
413 *Journal*, 18(1), 1–18. <https://doi.org/10.2136/vzj2018.12.0209>
- 414 Flinchum, B. A., Holbrook, W. S., & Carr, B. J. (2022). What Do P-Wave Velocities Tell Us
415 About the Critical Zone? *Frontiers in Water*, 3, 772185.
416 <https://doi.org/10.3389/frwa.2021.772185>
- 417 Gillieson, D., Wallbrink, P., & Cochrane, A. (1996). Vegetation change, erosion risk and land
418 management on the Nullarbor Plain, Australia. *Environmental Geology*, 28(3), 145–153.
419 <https://doi.org/10.1007/s002540050087>

- 420 Graham, R. C., Anderson, M. A., Sternberg, P. D., Tice, K. R., & Schoeneberger, P. J. (1997).
421 Morphology, Porosity, and Hydraulic Conductivity of Weathered Granitic Bedrock and
422 Overlying Soils. *Soil Science Society of America Journal*, 61(2), 516.
423 <https://doi.org/10.2136/sssaj1997.03615995006100020021x>
- 424 Gu, X., Heaney, P. J., Reis, F. D. A. A., & Brantley, S. L. (2020). Deep abiotic weathering of
425 pyrite. *Science*, 370(6515), eabb8092. <https://doi.org/10.1126/science.abb8092>
- 426 Hahm, W. J., Riebe, C. S., Lukens, C. E., & Araki, S. (2014). Bedrock composition regulates
427 mountain ecosystems and landscape evolution. *Proceedings of the National Academy of*
428 *Sciences*, 111(9), 3338–3343. <https://doi.org/10.1073/pnas.1315667111>
- 429 Hahm, W. J., Rempe, D. M., Dralle, D. N., Dawson, T. E., Lovill, S. M., Bryk, A. B., et al.
430 (2019). Lithologically Controlled Subsurface Critical Zone Thickness and Water Storage
431 Capacity Determine Regional Plant Community Composition. *Water Resources Research*,
432 55(4), 3028–3055. <https://doi.org/10.1029/2018wr023760>
- 433 Hayes, J. L., Riebe, C. S., Holbrook, W. S., Flinchum, B. A., & Hartsough, P. C. (2019).
434 Porosity production in weathered rock: Where volumetric strain dominates over chemical
435 mass loss. *Science Advances*, 5(9), eaao0834. <https://doi.org/10.1126/sciadv.aao0834>
- 436 He, S., Ohara, N., & Miller, S. N. (2019). Understanding subgrid variability of snow depth at 1-
437 km scale using Lidar measurements. *Hydrological Processes*, 33(11), 1525–1537.
438 <https://doi.org/10.1002/hyp.13415>

- 439 Holbrook, W. S., Riebe, C. S., Elwaseif, M., Hayes, J. L., Basler-Reeder, K., Harry, D. L., et al.
440 (2014). Geophysical constraints on deep weathering and water storage potential in the
441 Southern Sierra Critical Zone Observatory. *Earth Surface Processes and Landforms*, 39(3),
442 366–380. <https://doi.org/10.1002/esp.3502>
- 443 Huang, M., Hudson-Rasmussen, B., Burdick, S., Lekic, V., Nelson, M. D., Fauria, K. E., &
444 Schmerr, N. (2021). Bayesian Seismic Refraction Inversion for Critical Zone Science and
445 Near-Surface Applications. *Geochemistry, Geophysics, Geosystems*, 22(5).
446 <https://doi.org/10.1029/2020gc009172>
- 447 Keifer, I., Dueker, K., & Chen, P. (2019). Ambient Rayleigh wave field imaging of the critical
448 zone in a weathered granite terrane. *Earth and Planetary Science Letters*, 510, 198–208.
449 <https://doi.org/10.1016/j.epsl.2019.01.015>
- 450 Lebedeva, M. I., Fletcher, R. C., Balashov, V. N., & Brantley, S. L. (2007). A reactive diffusion
451 model describing transformation of bedrock to saprolite. *Chemical Geology*, 244(3–4), 624–
452 645. <https://doi.org/10.1016/j.chemgeo.2007.07.008>
- 453 Leone, J. D., Holbrook, W. S., Riebe, C. S., Chorover, J., Ferré, T. P. A., Carr, B. J., & Callahan,
454 R. P. (2020). Strong slope-aspect control of regolith thickness by bedrock foliation. *Earth*
455 *Surface Processes and Landforms*. <https://doi.org/10.1002/esp.4947>
- 456 Marston, R. A. (2010). Geomorphology and vegetation on hillslopes: Interactions, dependencies,
457 and feedback loops. *Geomorphology*, 116(3–4), 206–217.
458 <https://doi.org/10.1016/j.geomorph.2009.09.028>

- 459 McCormick, E. L., Dralle, D. N., Hahm, W. J., Tune, A. K., Schmidt, L. M., Chadwick, K. D., &
460 Rempe, D. M. (2021). Widespread woody plant use of water stored in bedrock. *Nature*,
461 597(7875), 225–229. <https://doi.org/10.1038/s41586-021-03761-3>
- 462 Navarre-Sitchler, A., Brantley, S. L., & Rother, G. (2015). How Porosity Increases During
463 Incipient Weathering of Crystalline Silicate Rocks. *Reviews in Mineralogy and Geochemistry*,
464 80(1), 331–354. <https://doi.org/10.2138/rmg.2015.80.10>
- 465 Pasquet, S., Wang, W., Chen, P., & Flinchum, B. A. (2021). Multiwindow weighted stacking of
466 surface-wave dispersion. *GEOPHYSICS*, 86(2), EN39–EN50.
467 <https://doi.org/10.1190/geo2020-0096.1>
- 468 Pedrazas, M. A., Hahm, W. J., Huang, M., Dralle, D., Nelson, M. D., Breunig, R. E., et al.
469 (2021). The Relationship Between Topography, Bedrock Weathering, and Water Storage
470 Across a Sequence of Ridges and Valleys. *Journal of Geophysical Research: Earth Surface*,
471 126(4). <https://doi.org/10.1029/2020jf005848>
- 472 Rempe, D. M., & Dietrich, W. E. (2018). Direct observations of rock moisture, a hidden
473 component of the hydrologic cycle. *Proceedings of the National Academy of Sciences*,
474 115(11), 2664–2669. <https://doi.org/10.1073/pnas.1800141115>
- 475 Rücker, C., Günther, T., & Wagner, F. M. (2017). pyGIMLi: An open-source library for
476 modelling and inversion in geophysics. *Computers & Geosciences*, 109, 106–123.
477 <https://doi.org/10.1016/j.cageo.2017.07.011>

- 478 Salve, R., Rempe, D. M., & Dietrich, W. E. (2012). Rain, rock moisture dynamics, and the rapid
479 response of perched groundwater in weathered, fractured argillite underlying a steep hillslope.
480 *Water Resources Research*, 48(11). <https://doi.org/10.1029/2012wr012583>
- 481 Schmidt, L., & Rempe, D. (2020). Quantifying Dynamic Water Storage in Unsaturated Bedrock
482 with Borehole Nuclear Magnetic Resonance. *Geophysical Research Letters*, 47(22).
483 <https://doi.org/10.1029/2020gl089600>
- 484 Smith, W. H. F., & Wessel, P. (1990). Gridding with continuous curvature splines in tension.
485 *Geophysics*, 55(3), 293–305. <https://doi.org/10.1190/1.1442837>
- 486 Uecker, R. K., Flinchum, B. A., Holbrook, W. S., & Carr, B. J. (2023). Mapping bedrock
487 topography: a seismic refraction survey and landscape analysis in the Laramie Range,
488 Wyoming. *Frontiers in Water*, 5, 1057725. <https://doi.org/10.3389/frwa.2023.1057725>
- 489 Uhlig, D., & Blanckenburg, F. von. (2019). How Slow Rock Weathering Balances Nutrient Loss
490 During Fast Forest Floor Turnover in Montane, Temperate Forest Ecosystems. *Frontiers in*
491 *Earth Science*, 7, 159. <https://doi.org/10.3389/feart.2019.00159>
- 492 Uhlig, D., Schuessler, J. A., Bouchez, J., Dixon, J. L., & Blanckenburg, F. von. (2017).
493 Quantifying nutrient uptake as driver of rock weathering in forest ecosystems by magnesium
494 stable isotopes. *Biogeosciences*, 14(12), 3111–3128. <https://doi.org/10.5194/bg-14-3111-2017>
- 495 Wang, W., Chen, P., Keifer, I., Dueker, K., Lee, E.-J., Mu, D., et al. (2019). Weathering front
496 under a granite ridge revealed through full-3D seismic ambient-noise tomography. *Earth and*
497 *Planetary Science Letters*, 509, 66–77. <https://doi.org/10.1016/j.epsl.2018.12.038>

